Non-linear behaviour and failure mechanism of bamboo poles in bending

Rodolfo Lorenzo[a*], Leonel Mimendi[a], Dong Yang[b], Haitao Li[b], Theodora Mouka[c], Elias G. Dimitrakopoulos[c]
[a] Department of Civil, Environmental and Geomatic Engineering, University College London, London WC1E 6BT, UK
[b] College of Civil Engineering, Nanjing Forestry University, Nanjing 210037, China
[c] Department of Civil and Environmental Engineering, The Hong Kong University of Science and Technology, Clear Water Bay, Kowloon, Hong Kong
*Corresponding author: r.lorenzo@ucl.ac.uk (R. Lorenzo)

Abstract

The adoption of bamboo poles in construction can support the reduction of carbon dioxide emissions generated by the manufacture of conventional structural elements produced from unsustainable industrialised materials. This research focuses on the study of the nonlinear softening behaviour and failure mechanism of bamboo poles in bending through a series of experimental tests on Moso (Phyllostachys pubescens) bamboo and Finite Element simulations supported by digitisation techniques. The results indicate that this nonlinear behaviour is caused by the incremental development of cracks at the locations where the circumferential tensile capacity of bamboo is exceeded leading to the eventual failure of the pole. Also, the simulations in this study suggest that reinforcing bamboo poles with pretensioned stainless steel bands is ineffective in counteracting the development of significant circumferential tensile stresses and the associated longitudinal cracks. More generally, this work highlights the challenges and limitations of applying traditional methods of structural testing and design for manufactured components to a highly variable natural structural element and speculates whether modern digital technologies can be adopted to manage more effectively the effects of this inherent variability.

Keywords:

Bamboo; Bending; Nonlinear behaviour; Failure mechanism

1. Introduction

Bamboo is a natural material that has received increasing attention during the last decades due to its sustainable and renewable characteristics along with its fast-growing [1] and carbon sequestration properties [2]. The implementation of bamboo poles in the architecture, engineering and construction industry has the potential to support the reduction of carbon dioxide emissions generated by the manufacture of the main conventional structural elements produced from steel or concrete [3]. However, there are still numerous challenges to manage the significant variability in geometric [4–6] and mechanical properties [7–9] to ensure an efficient use of this natural material while guaranteeing its structural reliability.

Historically, the bending behaviour of bamboo poles has been studied based on traditional experimental bending tests and Euler-Bernoulli theory [10]. Most studies assume bamboo to be an isotropic, straight and circular hollow element undergoing small deformations [8,11–16]. The practical challenges involved in the effective implementation of these traditional tests and the applicability of these assumptions on a highly organic and flexible orthotropic tube can be a potential compounding factor responsible for the wide variability of results and low design values for structural bamboo usually reported in the literature. This is particularly relevant to the study of bamboo poles in bending beyond their linear elastic limitwhich shows a clear nonlinear softening behaviour up to failure [4,14]. The latest ISO standard [17] assumes a lower bound value for this limit of proportionality at 60% of the ultimate load. Previous studies based on clear bamboo samples [7,18,19] do not show evidence of any significant ductility in the material itself and alternative mechanisms responsible for this nonlinearity have not been previously investigated. Furthermore, failure mechanisms have been traditionally attributed to axial crushing or buckling of the bamboo wall in compression or longitudinal splitting caused by tension or shear [20,21,22] as a simplification of the more complex experimental behaviour reported in the literature [8,11,13,16]. Moreover, the stresses developed due to these mechanisms at the linear elastic limit are significantly lower than the corresponding ultimate values of the material

[23], indicating that an alternative effect is responsible for the observed nonlinear behaviour of bamboo poles in bending. This paper is therefore focused on the assessment of these alternative effects to contribute to the understanding of this nonlinear behaviour and subsequent failure mechanism.

Apart from the development of the ultimate axial and shear stresses in bamboo poles in bending, other theoretical failure mechanisms and potential sources of nonlinearity in isotropic hollow tubes in bending include local and global buckling effects as well as the ovalization of the cross section (Brazier effect) as the curvature of the tube increases [24]. Theoretical studies on these same mechanisms incorporating the effect of material orthotropy have been more recently developed [25–27] along with multiple studies on the characterisation of bamboo as an orthotropic or, more precisely, transversely isotropic material [28–31]. As such, the stiffness and strength of bamboo in the circumferential and radial directions, which are significantly lower than the longitudinal ones [32,33], can have a significant effect on the behaviour of natural tubular structural elements [34].

This study presents an analytical assessment of the potential mechanisms responsible for the experimentally observed nonlinearity in third-point bending tests including the development of a refined Finite Element (FE) model to numerically simulate the poles' behaviour and compare it against experimental observations. This FE model is also adopted to simulate the effects of the commonly used steel banding on the behaviour of bamboo poles in bending. The results of a typical pole are used throughout this work to illustrate the general behaviour of bamboo poles in bending, the practical challenges in implementing a traditional third-point bending test and the effects of idealising their organic geometry as straight prismatic circular tubes. This approach deliberately deviates from the traditional statistical characterisation of bamboo to highlight the potential of modern digitisation techniques [35] and parametric numerical analyses as the basis of an alternative approach [36] to effectively quantify, model and study the structural behaviour of bamboo recognising each pole as a unique structural element.

2. Experimental programme

The experimental programme developed for this study included three main activities: i) digitisation of a sample of bamboo poles to generate geometrically accurate line and shell Finite Element (FE) models; ii) testing of small clear samples to estimate the poles' compressive elastic modulus, compressive strength and shear strength, all parallel to the fibres and iii) third-point bending tests to record the poles' bending behaviour up to failure.

2.1. Material

This study is based on a sample of ten, 4 m-long Moso (Phyllostachys pubescens) bamboo poles originating from Jiangsu, P. R. China. The poles' harvest age was four years and they were treated with a caramelisation process which involves piercing their nodal diaphragms with 10-20 mm perforations before placing them in a horizontal furnace for 90 minutes at 75°C, 45% humidity and 1.60 MPa followed by air-drying for 1 to 2 weeks. The poles were kept in a controlled laboratory environment for two weeks prior to their use as specified in ISO 22157 [17]. The moisture content of all samples was measured at the time of testing using a pre-calibrated handheld Delmhorst BD-2100 moisture meter [7]. Two of the ten poles were reinforced with 13 mm wide by 0.914 mm thick stainless steel (304) banding [37] arbitrarily spaced at around one diameter along their length and installed with a Bosch GDR 12V-105 impact driver.

2.2. Bamboo digitisation

All bamboo poles were digitised following the process described in [35] and [4] using the setup shown in Fig. 1. This process is based on the use of a hand-held three-dimensional (3D) Artec Eva scanner [38] with a resolution of 0.5 mm and a point accuracy of 0.1 mm. This scanner was operated with a laptop Dell XPS 15 equipped with an Intel i7-6700HQ CPU @ 2.66GHz, 16GB of installed memory and a dedicated video card Nvidia GTX GeForce 960m with 4GB of memory whilst the processing of point clouds was carried out in a workstation Dell Precision with an Intel Xeon E5-1620v3 CPU @ 3.5GHz, 32GB of memory and a dedicated video card Nvidia Quadro K2200 with 4GB of memory. The acquired point cloud was reconstructed into a polygon mesh [39] using Artec's proprietary software Artec Studio 14 [38] which in turn was reconstructed into the final Non-Uniform Rational B-Spline (NURBS) model and associated numerical data using a bespoke Python [40] script in Rhino3D [41] developed by [35].

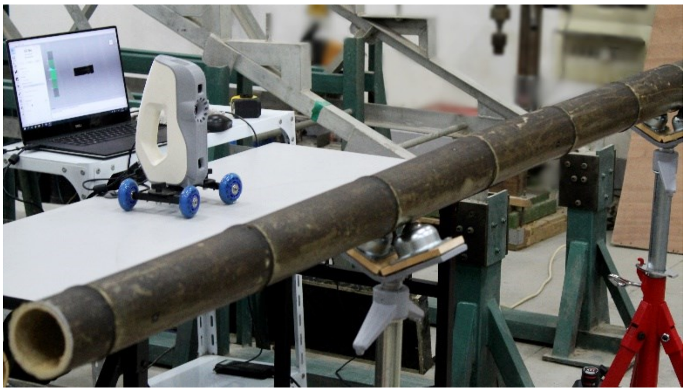

Fig. 1. 3D scanning set up

This NURBS-model provides an accurate and efficient representation of the geometry of each pole as illustrated in Fig. 2 for a typical pole (pole ML3). The numerical data extracted from the NURBS-model is the basis for the structural modelling of the poles. The discretisation of the poles into the analytical line models used in this study follows their anatomical features [35] and so these data include the position of the centroid at each nodal cross section as well as the section properties at the mid-internodes as described in [35] and schematically shown in Fig. 2. These section properties, including those corresponding to an equivalent circular tube, are given by [35]:

Cross sectional area, $A = A_o - A_i$ (1)

Equivalent outer diameter, $D = \sqrt{\frac{4A_o}{\pi}}$ (2)

Equivalent thickness, $t = \frac{D - \sqrt{D^2 - \frac{4A}{\pi}}}{2}$ (3)

Equivalent moment of inertia, $I = \frac{\pi}{64}[D^4 - (D - 2t)^4]$ (4)

Equivalent polar moment of inertia, $J = \frac{\pi}{32}[D^4 - (D - 2t)^4]$ (5)

Principal moments of inertia, $I_{1,2} = \frac{1}{2}\left[\left(I_y + I_z\right) \pm \sqrt{\left(I_z - I_y\right)^2 + 4I_{yz}^2}\right]$ (6)

Direction of principal moments of inertia, $\theta = \frac{1}{2}tan^{-1}\left(\frac{2I_{yz}}{I_z - I_y}\right)$ (7)

where: A_o and A_i are the cross-sectional areas of the outer and inner pole surfaces respectively and I_y, I_z and I_{yz} are the moments of inertia and product moment of inertia of the actual internodal cross section calculated directly from the NURBS model using the relevant Rhino3D function library.
On the other hand, the structural shell models adopted in this study are based on the NURBS mid-thickness surface discretised into a mesh of triangular elements as shown in Fig. 2 with individual thickness values determined from the digital models. The NURBS postprocessing and meshing was carried out based on Rhino3D and its visual programming plugin Grasshopper3D [42].

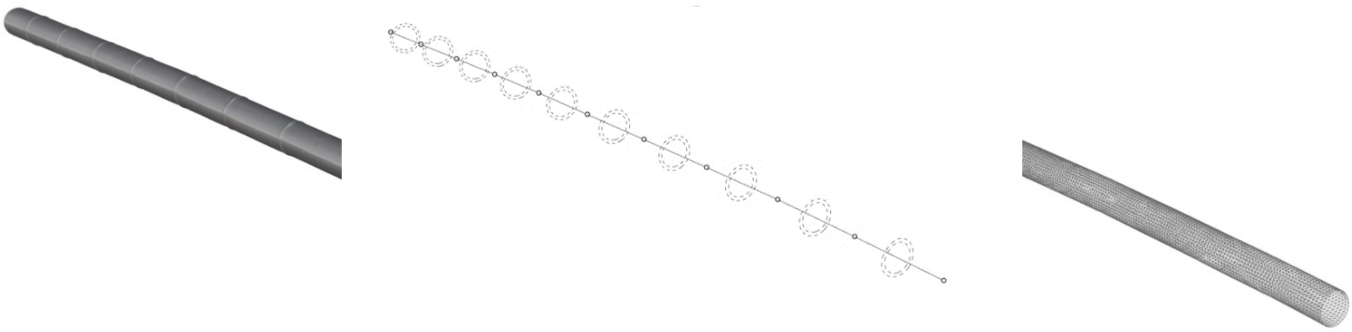

Fig. 2. NURBS model of pole ML3 (left) and its line (centre) and shell (right) Finite Element idealisations

2.2. Clear bamboo samples testing

Small clear bamboo samples were fabricated from the eight unreinforced poles to estimate their compressive elastic modulus (E_c), compressive strength (f_c) and shear strength (f_v), all parallel to the fibres, following the Chinese industry standard JG/T 199-2007 [43]. As shown in Fig. 3, two diametrically opposite sets of samples were robotically extracted from the internodes at each end of the 4 m-long bamboo poles according to the methodology described in [44]. All specimens were kept at a constant temperature of 20 °C ± 2 °C and relative humidity of 65% ± 5%. The test machine used for this study was an electro-mechanical, single column Instron 3345 with a maximum capacity of 5 kN with a clip-on strain gauge extensometer (model 2630). Compressive specimens requiring a higher load capacity were tested on a Controls UNIFLEX universal testing machine with a capacity of 300 kN. Average material properties for each pole were calculated from the four specimens extracted, adjusted to the moisture content of the corresponding pole at the time of the bending test.

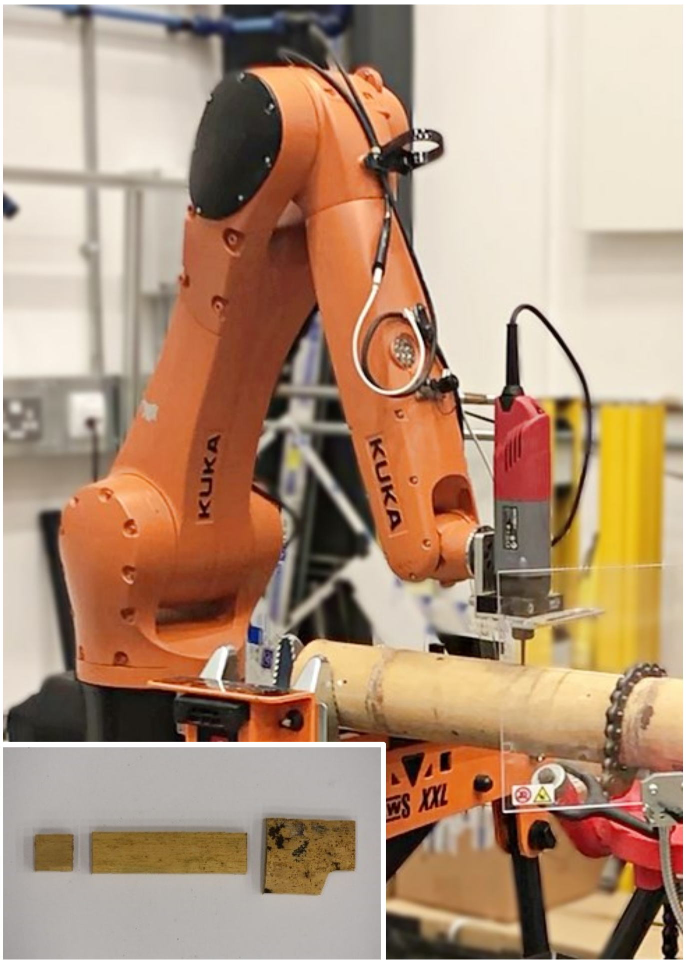

Fig. 3. Robotic fabrication of clear bamboo samples

The compressive strength parallel to the fibers, f_c, was calculated as [43]:

$$f_c = \frac{1}{n}\sum K_{f_c}\frac{P_c}{bt} \tag{8}$$

where n is the number of samples (four), P_c is the maximum applied load and b and t are the specimen width and thickness, respectively. K_{f_c} is a correction factor for the effect of moisture content developed from [43] as:

$$K_{f_c} = \frac{0.79+1.5e^{-0.16w}}{0.79+1.5e^{-0.16w_{fc}}} \tag{9}$$

where w and w_{f_c} are the moisture content of the bamboo poles and respective clear samples measured at the time of testing.

The elastic modulus parallel to the fibers, E_c, was calculated as [43]:

$$E_c = \frac{1}{n}\sum K_{E_c}\frac{\Delta\sigma_c}{\Delta\epsilon_c} \tag{10}$$

where $\Delta\sigma_c$ is the stress difference between the minimum (5 MPa) and maximum (20 MPa) stress limits and $\Delta\epsilon_c$ is the deformation difference measured at the stress limits after six loading and unloading cycles. K_{E_c} is a correction factor for the effect of moisture content developed from [43] as:

$$K_{E_c} = \frac{0.89+0.36e^{-0.1w}}{0.89+0.36e^{-0.1w_{E_c}}} \tag{11}$$

and w_{E_c} is the moisture content of the clear samples at the time of testing.

Finally, shear strength parallel to the fibre, f_v, was calculated as [43]:

$$f_v = \frac{1}{n}\sum K_{f_v}\frac{P_v}{lt} \tag{12}$$

here P_v is the maximum applied load, l and t are the length and thickness of the shear section respectively. K_{f_v} is a correction factor for the effect of moisture content developed from [43] as:

$$K_{f_v} = \frac{0.67+0.77e^{-0.07w}}{0.67+0.77e^{-0.07w_{f_v}}} \tag{13}$$

and w_{f_v} is the moisture content of the clear samples at the time of testing.

A summary of the clear bamboo sample testing results for the tested poles is shown in Table 1.

Pole	E_c (MPa)	f_c (MPa)	f_v (MPa)
MS1	13370	51.2	16.7
MS2	11630	49.3	15.9
MS3	13200	60.0	16.5
MS4	11570	52.4	16.9
ML1	10430	50.9	19.6
ML2	8810	43.9	16.3
ML3	11640	72.2	21.8
ML4	11900	60.8	20.0

Table 1. Test results of clear bamboo samples

2.3. Third-point bending testing

Third-point bending tests on all bamboo poles were carried out according to ISO 22157 [17] on a structural test system Popwill MAS-300 equipped with a 300 kN actuator, a laser displacement sensor SICK OD Precision OD5-500 W200 to record mid-span displacements and a data logger TML TDS-30. The clear span of all poles was set to 3 m complying with the minimum span requirements in ISO 22157. This standard also specifies the use of support and loading saddles to spread the loads circumferentially as evenly as possible around the top half of the pole and along its length to avoid crushing or kinking of the bamboo wall. Timber V-blocks with a straight 90° notch were used in this study including, when required, a protective 5 mm-thick neoprene layer placed between the pole and the timber saddles to avoid any localised damage by the blocks digging into the bamboo wall. These blocks were chosen over those with a curved notch as the latter are comparatively more difficult to fabricate and do not provide a significant improvement in terms of contact area with the pole due to its irregular, non-circular and tapering shape. None of the saddles were fixed to the loading frame in order to avoid introducing axial restraints during the tests.

Based on observations recorded during preliminary tests, two different loading saddle arrangements were adopted for this study as they led to two different failure mechanisms. The first arrangement (poles MS1 to MS4) consisted of two pairs of short, closely spaced, 37.5 mm-long saddles which produced a failure mechanism involving a gradual localised sharp kink with accompanying longitudinal splits concentrated under the loading saddles on the smaller half of the pole (Fig. 4). This same mechanism was previously identified as the predominant failure mode in an extensive study [16], which used fabric webbing of comparable width as the loading arrangement, indicating a similar effect on the circumferential load spread compared to timber saddles.

Fig. 4. Typical test setup and failure mode (inset) for short loading saddles

The second loading arrangement (poles ML1 to ML4) consisted of two longer 300 mm-long saddles required to avoid this localised kink and explore the second failure mechanism identified (Fig. 5). This mechanism involved the sudden development of longitudinal splits at the four quadrants of the poles extending along most of their length and originating within the main span to one side of the loading saddle on the smaller half of the pole.

Fig. 5. Typical test setup and failure mode (inset) for long loading saddles

Two additional tests (poles MLR1 and MLR2) were conducted on the poles reinforced with steel banding using 300 mm-long loading saddles (Fig. 6). In this case, the observed failure mechanism involved the development of splits in between bands on either side of the loading saddle on the smaller half of the pole, leading to the gradual formation of a localised kink.

Fig. 6. Typical test setup and failure mode (inset) for long loading saddles with reinforcement

The experimental load-displacement curves for all poles is shown in Fig. 7. Experimental testing results in bamboo poles include the effects of their natural variability and so it is particularly challenging to identify and measure the effects of varying parameters on their behaviour. This is the case for the saddle length in this study, which has a very clear qualitative effect that is not possible to isolate and quantify from the experimental results across different poles. In order to do so, this research adopts the use of refined numerical simulations and the experimental data described in this section to study the effect of varying parameters on the nonlinear softening behaviour displayed by all poles (Fig. 7).

The mechanical properties of the poles obtained from the third-point bending tests include the apparent modulus of elasticity in bending, $E_{\parallel}$, and the bending strength, $\sigma_{\parallel}$, both parallel to the direction of fibres, calculated as [17]:

$$E_{\parallel} = \frac{23(F_{60}-F_{20})L^3}{1296\, I_c(\Delta_{60}-\Delta_{20})} \tag{14}$$

$$\sigma_{\parallel} = \frac{F_{ult} L D_c}{12 I_c} \tag{15}$$

where F_{60} and F_{20} are the applied loads at 60% and 20% of the ultimate load, F_{ult}; Δ_{60} and Δ_{20} the corresponding mid-span deflections and L the clear span (3m). The outer diameter, D_c, and wall thickness, t_c, measured according to ISO 22157, are used to calculate the area, A_c, and moment of inertia I_c of the poles idealised as circular cylinders:

$$A_c = \frac{\pi}{4}\left[{D_c}^2 - (D_C - 2t_C)^2\right] \tag{16}$$

$$I_c = \frac{\pi}{64}\left[{D_c}^4 - (D_C - 2t_C)^4\right] \tag{17}$$

A summary of the bending test data and results, including the moisture content, w, measured at the time of the third-point bending tests, is presented in Table 2. A relatively wide dispersion of results is a common feature found in the mechanical testing of natural bamboo poles that can be partly responsible for the low characteristic values usually reported in the literature [7,8,21,45]. For instance, the mean and coefficient of variation of $E_{\parallel}$ and $\sigma_{\parallel}$ for the poles in this study are 12030 N/mm^2 (CoV=14%) and 64.5 N/mm^2 (CoV=12%) respectively.

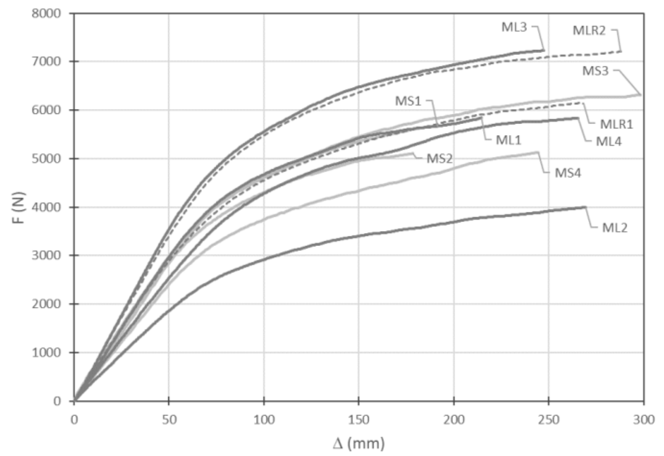

Fig. 7. Experimental load-displacement diagrams for third-point bending tests

Pole	D_c (mm)	t_c (mm)	A_c (mm²)	I_c (×10⁶ mm⁴)	w (%)	F_{ult} (kN)	$E_{\parallel}$ (N/mm²)	$\sigma_{\parallel}$ (N/mm²)
MS1	88.4	8.6	2162	1.741	14.2	5.67	15410	72.0
MS2	94.6	8.5	2300	2.153	15.5	5.11	11930	56.1
MS3	90.4	9.0	2308	1.935	13.5	6.32	13560	73.8
MS4	84.3	9.8	2283	1.612	13.4	5.13	12920	67.0
ML1	95.7	9.7	2631	2.461	11.7	5.84	11110	56.8
ML2	89.0	7.8	1979	1.647	13.2	3.99	9690	54.0
ML3	99.0	9.0	2541	2.601	9.1	7.23	12320	68.8
ML4	89.4	9.0	2263	1.851	13.8	5.84	12180	70.4
MLR1	95.0	8.4	2288	2.165	11.4	6.14	11250	67.4
MLR2	98.5	11.7	3198	3.068	12.3	7.21	9920	57.9

Table 2. Summary of third-point bending test results

The practical implementation of the bending test procedure described in ISO 22157 presents some challenges due to the organic geometry of bamboo which prevents, to varying degrees, the alignment of the pole, loading saddles and supports into one vertical plane as required by this standard. In addition, allowing the poles to "settle" into their own position as they are placed on the supports and/or come into contact with the loading saddles does not necessarily lead to a unique rest position due to their inherent three-dimensional geometric variability. These effects are illustrated in Fig. 8 which shows the top and front views of the digital model of a typical pole (ML3) in its final testing position found through the spatial correlation of physical markers placed on the poles and captured during the digitisation process. This figure includes reference centrelines passing through the pole centroids at the supports to highlight the positional shift of the loading saddles from this centreline whose position and orientation (tangential to the pole centroidal line) tend to follow the natural curvature of the poles. The contact area of some of the saddles (or similar devices) with the poles is also likely to be affected by the natural surface imperfections found in bamboo such as nodal ridges and branch scars.

Fig. 8. Alignment of saddles on a typical pole (ML3) in its testing position

The effect of the alignment and orientation of the poles on the results of third-point bending tests was explored through a series of parametric Finite Element (FE) analyses using the structural analysis software Karamba 3D [46]. These analyses were based on a line model of pole ML3 rotated about the supports centreline in Fig. 8 to simulate the effect of the pole "settling" in different positions. The pole curvature (out-of-straightness) was calculated from the digital model of this pole as the maximum distance between this centreline and its centroidal axis leading to a length:curvature ratio of 163 which is considered within the normal range by current design guidelines [47–50]. The elastic modulus in Table 2 and the actual section properties of the pole according to the discretisation shown in Fig. 2 were adopted for these analyses. In accordance with the findings of a previous study [4], significant differences were found between these section properties (Eqs. (1), (6) and (7)) and those of its idealised equivalent cylinder (Eqs. (16) and (17) and Table 2) as shown in Fig. 9 and typified by the irregular cross section in Fig. 10. The FE results at the upper limit of the linear range of the bending test (i.e. applied load, F_{60}) showed a difference in the maximum vertical displacement of up to 7% between different "settled" positions and 10% compared to the results of an idealised model of the pole based on the corresponding properties of a straight circular cylinder (Table 2). A 10% difference was also found between the maximum displacement of this idealised model and that of a model in which all minor axes of inertia were artificially aligned with a horizontal plane to simulate the effect of a hypothetical uniformly flat pole. The magnitude and significance of the effects of considering an idealised geometry for bamboo poles will vary from pole to pole not only due to their unique geometry but also their position within a structure. These effects can be a contributing factor to a wide range of issues found in structural bamboo from the common wide scatter of experimental test results to unacceptable construction tolerances that affect not only design values but also the quality and reliability of bamboo structures.

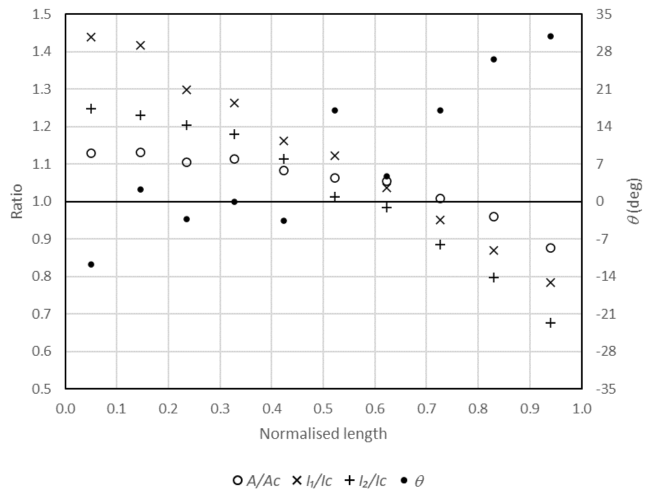

Fig. 9. Ratio of actual to cylindrical section properties for pole ML3

Fig. 10. Example of an irregular internodal cross-section

3. Nonlinear behaviour

The onset of the nonlinear softening behaviour in bamboo experimentally identified during the third-point bending tests occurs at approximately 60% of the ultimate load in agreement with the lower bound proportionality limit given in ISO 22157 [17]. A series of analytical calculations and numerical simulations were carried out to determine the predominant mechanism responsible for this nonlinearity. The relevant mechanisms examined in this study include failure or damage caused by: i) axial and longitudinal shear stresses; ii) ovalization; iii) local buckling and iv) circumferential tensile stresses.

3.1. Axial and longitudinal shear stresses

From basic bending theory [10], the maximum bending moment, M_{60}, and maximum axial, σ_{60}, and longitudinal shear, τ_{60}, stresses developed in the idealised bamboo poles at the proportionality limit are:

$$M_{60} = \frac{F_{60}L}{6} \tag{18}$$

$$\sigma_{60} = \frac{M_{60}D_c}{2I_c} \tag{19}$$

$$\tau_{60} = \frac{F_{60}}{\pi D_c t} \tag{20}$$

Table 3 shows the ratio between these stresses and the compression (f_c) and shear (f_v) capacity of the clear bamboo samples in Table 1 taken as reference. These ratios are all significantly less than one indicating that neither crushing nor longitudinal shear splitting are responsible for the observed nonlinear behaviour in the bending tests.

3.2 Ovalization

The combination of longitudinal stresses and curvature in a thin-walled tube in bending tends to flatten its cross section into an oval shape reducing its flexural stiffness [24]. This ovalization, or Brazier effect, is quantified through a maximum moment, M_{max}, which, for an orthotropic tube, is given by [26]:

$$M_{max} = \frac{\pi\sqrt{2}}{9} D_c t_c^2 \sqrt{E_{\parallel} E_{\perp}} \tag{21}$$

where $E_{\perp}$ is the transverse elastic modulus of Moso bamboo taken as 1360 MPa according to the study conducted by [29]. The low ratio between M_{60} and M_{max} for all poles shown in Table 3 also indicate that ovalization is not a critical mechanism in bamboo poles in bending.

3.3 Local buckling

The critical moment, M_{cr}, for local buckling in bamboo poles, based on classical bifurcation buckling theory for cylindrical shells incorporating the effect of ovalization and the orthotropic nature of bamboo poles, is given by [24,27]:

$$M_{cr} = \frac{s_{cr}\pi}{2\sqrt{3}} D_c t_c^2 \sqrt{E_{\parallel} E_{\perp}} \tag{22}$$

where s_{cr} is a non-dimensional factor equal to 0.564. By inspection, local buckling is also not considered a critical mechanism based on the low ratio between M_{60} and M_{cr} shown in Table 3.

Pole	σ_{60}/f_c	τ_{60}/f_v	M_{60}/M_{max}	M_{60}/M_{cr}
MS1	0.84	0.09	0.11	0.11
MS2	0.68	0.08	0.11	0.11
MS3	0.74	0.10	0.12	0.12
MS4	0.77	0.08	0.09	0.09
ML1	0.67	0.07	0.10	0.10
ML2	0.74	0.07	0.12	0.12
ML3	0.57	0.08	0.13	0.13
ML4	0.70	0.08	0.12	0.12

Table 3. Analytical results for bending stresses, ovalization and local buckling

3.4 Circumferential tensile stresses

The unidirectional (axial) alignment of fibres in bamboo poles is responsible for their low tensile capacity in the circumferential direction and therefore a series of shell Finite Element (FE) analyses were conducted to assess the role of tensile circumferential stresses, $\sigma_{t\perp}$, on the observed nonlinear behaviour of bamboo poles in third-point bending. These analyses were performed on the structural analysis software Karamba3D (Karamba3D, 2020), which is based on flat *TRIC* shell elements without shear deformations [51], adopting an orthotropic material model with longitudinal and transverse elastic moduli, $E_{\parallel}$ and $E_{\perp}$, as previously defined in Eqs (14) and (21) respectively. The shell model adopted for this study is based on the digitised geometry of pole ML3 which, following the results of a sensitivity analysis, was discretised into a mid-thickness mesh of triangular elements with a maximum edge length of approximately 10 mm and individual thickness values extracted from the NURBS model at the centroid of each element. This same model was also used to study the effect of reinforcing steel banding (Fig. 6) uniformly distributed along the length of the pole. These bands were modelled as a ring of pre-tensioned 13 mm × 0.914 mm stainless steel beam elements with an elastic modulus of 200,000 MPa whose geometry follows the external surface of the NURBS model of the pole and are radially connected to the mid-thickness mesh through rigid links with released rotational restraints. It is not practically possible to accurately quantify the prestress in the bands and therefore the analysis assumed a prestress equal to the yield stress of the bands (230 MPa) as an initial upper bound value.

As expected, the maximum mid-span displacement, Δ_{60}, for all models at the proportionality limit (i.e. applied load F_{60} = 4.34 kN) closely matches the experimental data shown in Fig. 11.

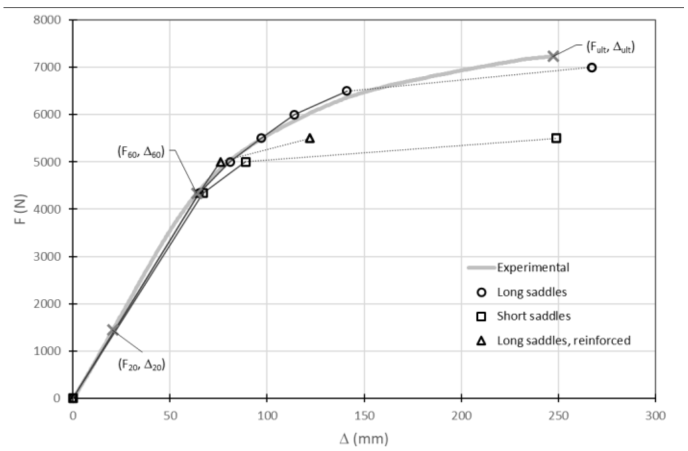

Fig. 11. Experimental and numerical load-displacement diagram for pole ML3

At this proportionality limit, the tensile circumferential stresses on the inside wall, $\sigma_{ti\perp}$, are higher than on the outside reaching a maximum value under the applied loads as shown in Fig. 12 for the models with long (300 mm) loading saddles, as in the experimental test, and short (37.5 mm) ones. This figure also includes the results of pole ML3 modelled with long (300 mm) loading saddles and prestressed steel banding as reinforcement.

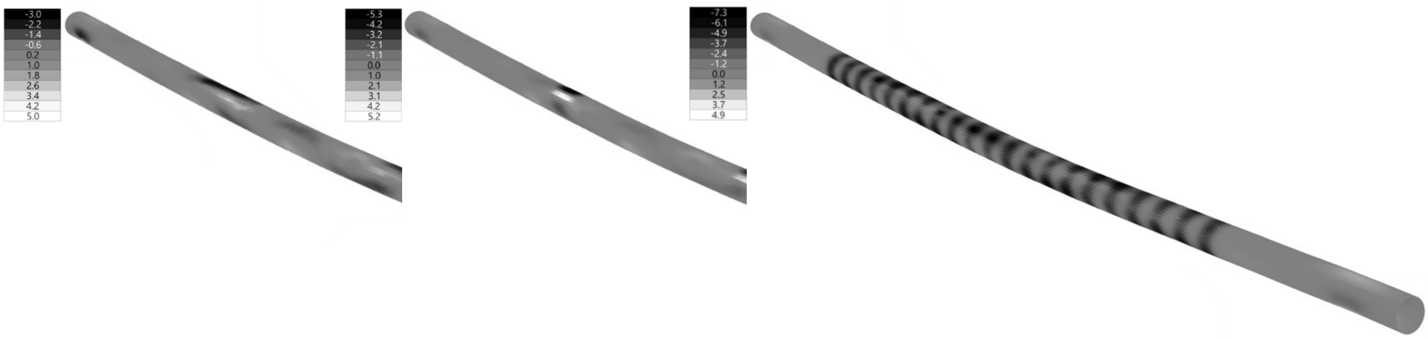

Fig. 12. $\sigma_{ti\perp}$ for pole ML3 with long (left, right) and short (centre) loading saddles and reinforcement (right)

The effect of the actual pole geometry is evident in the irregular stress distribution shown in Fig. 12 compared with the purely academic stress distribution (perfectly symmetric without any localised peaks) in the corresponding idealised model of an average cylindrical tube with 300 mm loading saddles in Fig. 13.

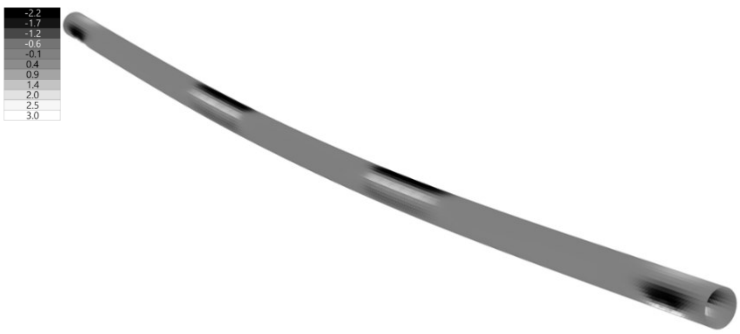

Fig. 13. $\sigma_{ti\perp}$ of idealised pole ML3 with long loading saddles

The maximum circumferential tensile stress of 3 MPa in this idealised model was adopted as an average value of the circumferential tensile capacity of the pole under the hypothesis that the nonlinear softening behaviour displayed after the proportionality limit is due to the incremental development of cracks at the locations where this capacity is exceeded during the bending test. The clearly noticeable continuous “clicking” sounds emitted by the pole during the tests qualitatively align with this hypothesis. The incremental development of cracks along the pole was simulated through a series of iterative analyses, analogous to those in Evoultionary Structural Optimisation [52], as follows:

1. Model analysed at load F_{60}
2. Shell elements with $\sigma_{t\perp} > 3\ MPa$ identified and assigned a nominal elastic modulus (i.e. “soft kill”)
3. Steps 1 and 2 repeated until $\sigma_{t\perp} < 3\ MPa$ for all shell elements verifying, as reference, that f_c is not exceeded
4. Model updated using deformed geometry, corresponding internal strains and soft killed elements
5. Updated model analysed for a load increment of approximately 500 N
6. Steps 2 to 5 repeated until an equilibrium condition in which $\sigma_{t\perp} < 3\ MPa$ could not be found

Only linear elastic analyses were carried out based on sensitivity tests which showed no significant differences with nonlinear geometric analyses.

The results obtained for the three configurations considered are shown in Fig. 11. The simulation for the testing configuration with 300 mm-long loading saddles closely follows the experimental curve, indicating that progressive damage through the development of cracks along the pole is a significant factor in the observed nonlinear softening behaviour. The circumferential tensile stresses, $\sigma_{ti\perp}$ and $\sigma_{to\perp}$, on the inside and outside of the pole in the final state of equilibrium found is shown in Fig. 14 for an applied load of 6.5 kN including all areas of predicted damage where the circumferential tensile capacity has been exceeded. The maximum axial compressive stress at this stage was 71.8 MPa which is just below the clear samples crushing strength of 72.2 MPa (Table 1). Fig. 14 also shows the pole configuration at 7 kN corresponding to the last point in the load-displacement plot in Fig. 11 for which no equilibrium state was reached but illustrates the expected deformed shape at failure. In line with experimental observations, signs of damage started developing within the span next to the loading saddle on the smaller half of the pole immediately followed by the development of longitudinal cracks in the four quadrants of the pole (Fig. 5) in agreement with the circumferential tensile stress distribution before failure at 6.5 kN shown in Fig. 14.

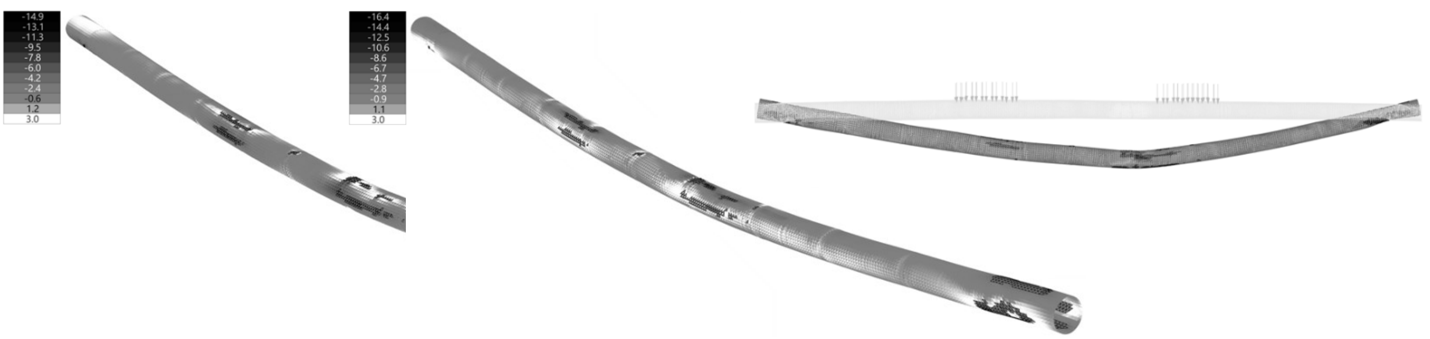

Fig. 14. $\sigma_{ti\perp}$ (left), $\sigma_{to\perp}$ (centre) and failure mode (right) for pole ML3 with long loading saddles

In contrast, the results for the short 37.5 mm-long loading saddles in Fig. 11 show the final state of equilibrium at 5kN and a limited dispersion of damage along the pole evident in the concentrated circumferential stress distribution in Fig. 15. The approximate failure configuration at 5.5 kN in this figure, for which no equilibrium state was reached, is also in line with experimental observations with a distinct sharp kink occurring under the loading saddle on the smaller half of the pole (Fig. 4).

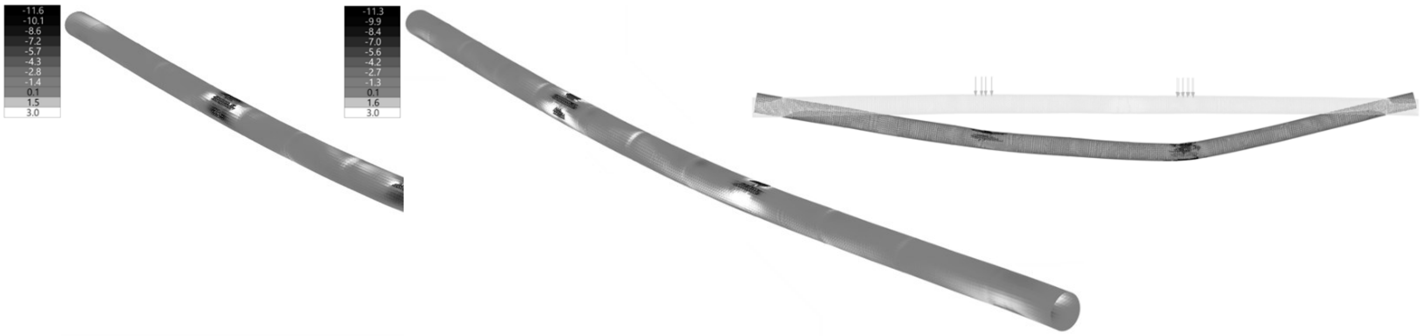

Fig. 15. $\sigma_{ti\perp}$ (left), $\sigma_{to\perp}$ (centre) and failure mode (right) for pole ML3 with short loading saddles

The results of the simulation with 300 mm-long loading saddles and reinforcing steel bands in Fig. 11 show a short continuation of the linear response of the system up to the final state of equilibrium found at the lower load of 5 kN compared to the unreinforced pole. Even under the assumed maximum prestress (yield stress), these results suggest that banding has a detrimental effect on the behaviour of the system. This can be partly explained by the high circumferential tensile stresses developed due to the cross-sectional deformation of the pole, combined with the residual prestress in the bands. This residual prestress seems to be sufficient to have an adverse effect on the system even considering the rapid loss of prestress from only 3% at the end of the proportionality limit to almost 50% at 5kN. Fig. 16 shows the concentration of circumferential tensile stresses along the pole and the approximate failure configuration at 5.5 kN, for which no equilibrium state was reached, demonstrating the agreement with the localised failure between bands evident during the experimental tests (Fig. 6).

Fig. 16. $\sigma_{ti\perp}$ (left), $\sigma_{to\perp}$ (centre) and failure mode (right) for reinforced pole ML3 with long loading saddles

In line with previous studies [15], no beneficial effect from the bamboo nodal diaphragms was identified in any of the experimental tests with cracks and general damage developing unimpeded through the nodes. This behaviour agrees with the maximum theoretical spacing for internal stiffeners required to avoid ovalization in orthotropic tubes given by [26]:

$$s = \left(\frac{E_{\perp}}{E_{\parallel}}\right)^{\frac{1}{4}} \sqrt{\frac{(D_c - t_c)^3}{32 t_c}} \qquad (23)$$

The theoretical values calculated for all tested poles range from 21 to 29 mm, which indicates that the much larger nodal spacing commonly found in bamboo poles renders their internal diaphragms ineffective at providing any significant beneficial effect on their structural behaviour.

The general bending behaviour studied in this work also extends to bamboo poles under axial loads due to the inherent geometric imperfections in these natural structural elements. As an illustration, the shell model of pole ML3 was analysed under axial compression with both ends restrained in translation except for the axial translation at the loaded end of the pole. Due to the nature of this problem, a nonlinear geometric analysis (Newton Raphson algorithm [51]) was performed noting that no true axial direction exists in bamboo poles due to the continuous spatial deviation of their centroidal axis from a straight line. The axial direction in this study, therefore, refers to the direction of a best-fit line through the digitally computed nodal centroids of the pole which minimises the eccentricities along its length. Even in this favourable orientation, Fig. 17 shows the significant out-of-plane deformation of the pole under axial compression together with the longitudinal, σ, and circumferential, $\sigma_{ti\perp}$ and $\sigma_{to\perp}$, stress distributions for a load of 46 kN. Under this load, the pole reaches the assumed tensile circumferential capacity of 3 MPa, when cracks are expected to start developing, and a maximum longitudinal compressive stress of 67.2 MPa close to the clear samples crushing strength of 72.2 MPa (Table 1). For reference, a maximum theoretical compressive load of 183 kN would be required to reach this crushing strength if the pole was idealised as a straight circular cylinder (Table 2). Evidently, the influence of eccentricities will vary for different poles but even the results of a single pole are highly dependent on its orientation as well as the load position and direction.

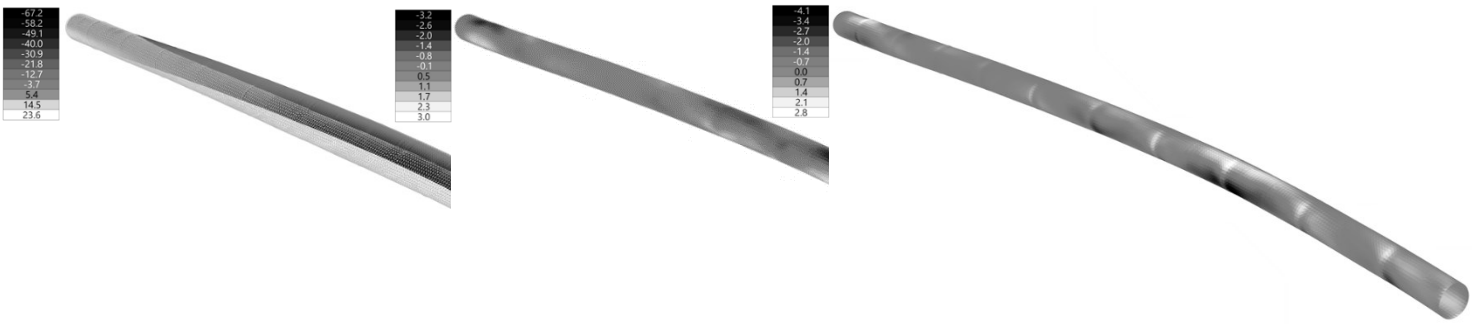

Fig. 17. σ (left), $\sigma_{ti\perp}$ (centre), $\sigma_{to\perp}$ (right) for pole ML3 in axial compression

4. Conclusion

The nonlinear softening behaviour of bamboo poles in bending beyond the proportionality limit (approximately 60% of the ultimate load) was studied through a series of experimental third-point bending tests and supported by digitisation techniques as well as robotic fabrication and mechanical testing of clear bamboo samples. The effects of three mechanisms potentially responsible for this nonlinearity were quantified through analytical assessments showing that bending (axial and longitudinal shear) stresses, ovalization and local buckling are not critical mechanisms. On the contrary, the results of iterative numerical simulations show that this nonlinear behaviour is likely caused by the incremental development of cracks at the locations where the circumferential tensile capacity of bamboo is exceeded, leading to the eventual failure of the pole. Different failure mechanisms were identified during the tests, that depend on the load dispersion achieved by the loading saddles including a sharp kink gradually forming under short 37.5 mm saddles and four longitudinal cracks almost instantly developing along most of the pole for longer 300 mm saddles. Both saddle configurations were included in the numerical simulations which managed to estimate the deformed shape at failure identified in the experimental tests. These simulations also included the analysis of poles reinforced with uniformly spaced, prestressed stainless steel bands which reproduced the experimentally observed failure caused by cracks concentrated in between bands. This suggests that this reinforcing approach is ineffective in counteracting the development of significant circumferential tensile stresses in the pole. This study shows the importance of quantifying the effect of circumferential tensile stresses not only in bending tests but also in the design and testing of structural systems and their connections to evaluate their significance in the failure mechanism of bamboo poles.

More generally, this work highlights the challenges and limitations of applying traditional methods of structural testing and design for manufactured components to a highly variable natural structural element. Due to this variability, assuming average geometric and mechanical properties for bamboo poles is likely to lead to excessive design factors for a material which, in absolute terms, is already significantly more flexible and weaker than its industrialised counterparts. Moreover, the inability to accurately quantify this variability can potentially lead to issues such as stress concentrations, unacceptable construction tolerances and other factors which can negatively affect the quality and reliability of a structure. The digital scanning and modelling, reverse engineering, robotic fabrication and parametric analysis techniques adopted for this study can be regarded as a speculative alternative approach to more effectively manage the effects of the inherent variability of bamboo poles to ensure their structural reliability.

Acknowledgements

Funding: This work was supported by the UK Engineering and Physical Sciences Research Council (EPSRC) [grant numbers: EP//M017702/1 & EP/P510890/1]; and the British Council/CSC UK-China Joint Research and Innovation Partnership Fund [grant number: UK-276080305].

References

[1] W. Liese, Research on bamboo, Wood Sci. Technol. 21 (1987) 189–209.

[2] W. Wu, Q. Liu, Z. Zhu, Y. Shen, Managing Bamboo for Carbon Sequestration, Bamboo Stem and Bamboo Shoots, Small-Scale For. 14 (2015) 233–243. https://doi.org/10.1007/s11842-014-9284-4.

[3] GABC, Global status report for buildings and construction- Towards a zero-emissions, efficient and resilient buildings and construction sector, Nairobi, Kenya, 2020. https://globalabc.org/sites/default/files/inline-files/2020 Buildings GSR_FULL REPORT.pdf (accessed January 8, 2021).

[4] R. Lorenzo, L. Mimendi, M. Godina, H. Li, Digital analysis of the geometric variability of Guadua, Moso and Oldhamii bamboo, Constr. Build. Mater. 236 (2020) 117535. https://doi.org/10.1016/j.conbuildmat.2019.117535.

[5] K.A. Harries, J. Bumstead, M. Richard, D. Trujillo, Geometric and material effects on bamboo buckling behaviour, Proc. Inst. Civ. Eng. - Struct. Build. 170 (2017) 236–249. https://doi.org/10.1680/jstbu.16.00018.

[6] K. Ghavami, L.E. Moreira, The influence of initial imperfections on the buckling of bamboo columns, Asian J. Civ. Eng. (Buillding Housing). 3 (2002) 1–16.

[7] R. Lorenzo, M. Godina, L. Mimendi, H. Li, Determination of the physical and mechanical properties of moso, guadua and oldhamii bamboo assisted by robotic fabrication, J. Wood Sci. 66 (2020) 20. https://doi.org/10.1186/s10086-020-01869-0.

[8] K.F. Chung, W.K. Yu, Mechanical properties of structural bamboo for bamboo scaffoldings, Eng. Struct. 24 (2002) 429–442. https://doi.org/10.1016/S0141-0296(01)00110-9.

[9] T.Y. Lo, H.Z. Cui, P.W.C. Tang, H.C. Leung, Strength analysis of bamboo by microscopic investigation of bamboo fibre, Constr. Build. Mater. 22 (2008) 1532–1535. https://doi.org/10.1016/j.conbuildmat.2007.03.031.

[10] R.C. Hibbeler, Mechanics of materials, 10th ed., Pearson Education Inc, Hoboken, New Jersey, 2017.

[11] N.M. Daud, N.M. Nor, M.A. Yusof, A.A.M. Al Bakhri, A.A. Shaari, The physical and mechanical properties of treated and untreated Gigantochloa Scortechinii bamboo, in: AIP Conf. Proc., 2018: p. 020016. https://doi.org/10.1063/1.5022910.

[12] N. Nugroho, E. Tri Bahtiar, Bamboo taper effect on third point loading bending test, Int. J. Eng. Technol. 5 (2013) 2379–2384.

[13] Nurmadina, N. Nugroho, E.T. Bahtiar, Structural grading of Gigantochloa apus bamboo based on its flexural properties, Constr. Build. Mater. 157 (2017) 1173–1189. https://doi.org/10.1016/j.conbuildmat.2017.09.170.

[14] R.A. Sá Ribeiro, M.G. Sá Ribeiro, I.P.A. Miranda, Bending strength and nondestructive evaluation of structural

bamboo, Constr. Build. Mater. (2017). https://doi.org/10.1016/j.conbuildmat.2017.04.074.

[15] D. Taylor, B. Kinane, C. Sweeney, D. Sweetnam, P. O'Reilly, K. Duan, The biomechanics of bamboo: investigating the role of the nodes, Wood Sci. Technol. 49 (2015) 345–357. https://doi.org/10.1007/s00226-014-0694-4.

[16] D. Trujillo, S. Jangra, J.M. Gibson, Flexural properties as a basis for bamboo strength grading, Proc. Inst. Civ. Eng. - Struct. Build. 170 (2017) 284–294. https://doi.org/10.1680/jstbu.16.00084.

[17] BSI ISO 22157, British adoption for International Standard Organization ISO 22157: 2019 Bamboo structures - Determination of physical and mechanical properties of bamboo culms - Test methods, (2019) 25. https://www.iso.org/standard/65950.html.

[18] Z.P. Shao, C.H. Fang, S.X. Huang, G.L. Tian, Tensile properties of Moso bamboo (Phyllostachys pubescens) and its components with respect to its fiber-reinforced composite structure, Wood Sci. Technol. 44 (2010) 655–666. https://doi.org/10.1007/s00226-009-0290-1.

[19] P.G. Dixon, L.J. Gibson, The structure and mechanics of Moso bamboo material, J. R. Soc. Interface. 11 (2014). https://doi.org/10.1098/rsif.2014.0321.

[20] M.J. Vaessen, J.J.A. Janssen, Analysis of the critical length of culms of bamboo in four-point bending tests, Heron. 42 (1997) 113–124. www.tue.nl/taverne (accessed April 13, 2020).

[21] D. Trujillo, Grading of Bamboo, Beijing, China, 2016. http://www.inbar.int/sites/default/files/Grading of bamboo_0.pdf (accessed July 28, 2021).

[22] J. Janssen, Bamboo in Building Structures, doctoral thesis, Eindhoven University of Technology, 1981.

[23] R. Lorenzo, L. Mimendi, H. Li, D. Yang, Bimodulus bending model for bamboo poles, Constr. Build. Mater. 262 (2020) 120876. https://doi.org/10.1016/j.conbuildmat.2020.120876.

[24] C.R. Calladine, Theory of Shell Structures, Cambridge University Press, 1983. https://doi.org/10.1017/CBO9780511624278.

[25] Y.-S. Huang, F.-L. Hsu, C.-M. Lee, J.-Y. Juang, Failure mechanism of hollow tree trunks due to cross-sectional flattening, R. Soc. Open Sci. 4 (2017) 160972. https://doi.org/10.1098/rsos.160972.

[26] U.G.K. Wegst, M.F. Ashby, The structural efficiency of orthotropic stalks, stems and tubes, J. Mater. Sci. 42 (2007) 9005–9014. https://doi.org/10.1007/s10853-007-1936-8.

[27] M. Paschero, M.W. Hyer, Axial buckling of an orthotropic circular cylinder: Application to orthogrid concept, Int. J. Solids Struct. 46 (2009) 2151–2171. https://doi.org/10.1016/j.ijsolstr.2008.08.033.

[28] Y. Akinbade, K.A. Harries, C. V. Flower, I. Nettleship, C. Papadopoulos, S. Platt, Through-culm wall mechanical behaviour of bamboo, Constr. Build. Mater. (2019). https://doi.org/10.1016/j.conbuildmat.2019.04.214.

[29] R. Moran, K. Webb, K. Harries, J.J. García, Edge bearing tests to assess the influence of radial gradation on the transverse behavior of bamboo, Constr. Build. Mater. 131 (2017) 574–584. https://doi.org/10.1016/j.conbuildmat.2016.11.106.

[30] L.A. Torres, K. Ghavami, J.J. García, A transversely isotropic law for the determination of the circumferential young's modulus of bamboo with diametric compression tests, Lat. Am. Appl. Res. 37 (2007) 255–260.

[31] J.J. Garcia, C. Rangel, K. Ghavami, Experiments with rings to determine the anisotropic elastic constants of bamboo, Constr. Build. Mater. 31 (2012) 52–57. https://doi.org/10.1016/j.conbuildmat.2011.12.089.

[32] B. Sharma, K.A. Harries, K. Ghavami, Methods of determining transverse mechanical properties of full-culm bamboo, Constr. Build. Mater. 38 (2013) 627–637. https://doi.org/10.1016/j.conbuildmat.2012.07.116.

[33] E.C.N. Silva, M.C. Walters, G.H. Paulino, Modeling bamboo as a functionally graded material: Lessons for the analysis of affordable materials, J. Mater. Sci. 41 (2006) 6991–7004. https://doi.org/10.1007/s10853-006-0232-3.

[34] K. Schulgasser, A. Witztum, On the strength, stiffness and stability of tubular plant stems and leaves, J. Theor. Biol. 155 (1992) 497–515. https://doi.org/10.1016/S0022-5193(05)80632-0.

[35] R. Lorenzo, L. Mimendi, Digitisation of bamboo culms for structural applications, J. Build. Eng. 29 (2020) 101193. https://doi.org/10.1016/j.jobe.2020.101193.

[36] R. Lorenzo, C. Lee, J.G. Oliva-Salinas, M.J. Ontiveros-Hernandez, BIM Bamboo: a digital design framework for bamboo culms, Proc. Inst. Civ. Eng. - Struct. Build. 170 (2017) 295–302. https://doi.org/10.1680/jstbu.16.00091.

[37] Jubilee Clips, (2021). https://www.jubileeclips.co.uk/assets/uploads/2019/02/Lit-Jubilee-Original-Range.pdf (accessed July 27, 2021).

[38] Artec 3D, (2021). https://www.artec3d.com/ (accessed February 17, 2021).

[39] Wikipedia, Polygon Mesh, (2019). https://en.wikipedia.org/wiki/Polygon_mesh (accessed January 24, 2019).

[40] PSF, Python Software Foundation. Software Version 3.5.1, (2015).

[41] RMNA, Robert McNeel & Associates- Rhinoceros 3D. Software Version 5.0, (2015).

[42] Grasshopper, Grasshopper, (2021). https://www.grasshopper3d.com/ (accessed July 24, 2021).

[43] MCBI, Ministry of Construction and Building Industry. MCBI: JG/t 199: 2007. Testing methods for the physical and mechanical properties of bamboo materials used in construction industry, (2007) 1–47.

[44] R. Lorenzo, M. Godina, L. Mimendi, H. Li, Determination of the physical and mechanical properties of moso, guadua and oldhamii bamboo assisted by robotic fabrication, J. Wood Sci. 66 (2020) 20. https://doi.org/10.1186/s10086-020-01869-0.

[45] S. Kaminski, A. Lawrence, D. Trujillo, I. Feltham, L.F. Lopez, Structural use of bamboo Part 3 : Design values, Struct. Eng. 94 (2016) 42–45.

[46] Karamba3D, Karamba3D – parametric engineering, (2020). https://www.karamba3d.com/#projects (accessed July 24, 2020).

[47] NSR-10 G, Reglamento Colombiano de Construcción Sismo Resistente. Título G. Estructuras de Madera y Estructuras de Guagua, (2010).

[48] ISO 22156, International Standard Organization ISO 22156. Bamboo - Structural design, (2021).

[49] J. Moran, Construir con Bambú Manual de construcción, 3rd ed., INBAR, 2015, 2015.

[50] S. Kaminski, A. Lawrence, D. Trujillo, I. Feltham, L.F. López, Structural use of bamboo. Part 4: Element design equations, Struct. Eng. 95 (2017) 24–27.

[51] Karamba3D Manual – Karamba3D, (2021). https://manual.karamba3d.com/ (accessed July 27, 2021).

[52] X. Huang, Y.M. Xie, Evolutionary Topology Optimization of Continuum Structures: Methods and Applications, John Wiley and Sons, 2010. https://doi.org/10.1002/9780470689486.